

## Article

# Controls on Critical Metal Enrichments in Ferromanganese Nodules from the Philippine Sea, at Water Depths of 4400–6000 m

Chao Li <sup>1</sup>, Weiyu Song <sup>2,3,\*</sup>, Zhenjun Sun <sup>4</sup>, Gang Hu <sup>2,3</sup>, Xiaojun Yuan <sup>2,3</sup> and Shuh-Ji Kao <sup>1,5,\*</sup>

<sup>1</sup> State Key Laboratory of Marine Environmental Science, College of Ocean and Earth Sciences, Xiamen University, Xiamen 361102, China

<sup>2</sup> Qingdao Institute of Marine Geology, China Geological Survey, Qingdao 266237, China

<sup>3</sup> Laboratory for Marine Mineral Resource, Pilot National Laboratory for Marine Science and Technology (Qingdao), Qingdao 266237, China

<sup>4</sup> School of Earth Sciences, Institute of Disaster Prevention, Sanhe 065201, China

<sup>5</sup> State Key Laboratory of Marine Resources Utilization in South China Sea, Hainan University, Haikou 570228, China

\* Correspondence: sweiyu@mail.cgs.gov.cn (W.S.); sjkao@xmu.edu.cn (S.-J.K.)

**Abstract:** Enrichments of critical metals in ferromanganese (Fe–Mn) nodules have received increasing attention in both deep-sea research and mineral exploration. To better assess the controls on the resource potential of Fe–Mn nodules, we conducted a comprehensive and detailed study of twelve nodules from the Philippine Sea collected from water depths of 4400 to 6000 m by investigating their microstructures, bulk geochemistry, and in situ Fe–Mn oxyhydroxide geochemistry, using XRF, ICP-MS, EMPA, and LA-ICP-MS coupled with BSE images. We successfully resolved different controls on the element enrichments, of which significant selective enrichment of metal elements in seawater is similar to that of typical hydrogenetic nodules. An enhanced supply of iron hydroxide due to calcite dissolution resulted in a dilution effect on Co, Ni, and Mn but an enrichment effect on rare earth elements plus yttrium (REE + Y) and Fe in nodules near topographic highs close to the carbonate compensation depth. While the supply of diagenetic Mn resulted in a dilution on Co and REE + Y, it resulted in enrichment on Ni, Cu, Li, and Mn on nodules on the seafloor. Moreover, via micro-layer analyses we confirmed the growth rate is a major determinant for the correlations of Co and REE with Fe-oxyhydroxides in these Philippine Sea nodules.

**Keywords:** ferromanganese nodules; critical metals; the Philippine Sea; high-resolution analysis



**Citation:** Li, C.; Song, W.; Sun, Z.; Hu, G.; Yuan, X.; Kao, S.-J. Controls on Critical Metal Enrichments in Ferromanganese Nodules from the Philippine Sea, at Water Depths of 4400–6000 m. *Minerals* **2023**, *13*, 522. <https://doi.org/10.3390/min13040522>

Academic Editor: Francisco J. González

Received: 19 March 2023

Revised: 3 April 2023

Accepted: 4 April 2023

Published: 7 April 2023



**Copyright:** © 2023 by the authors. Licensee MDPI, Basel, Switzerland. This article is an open access article distributed under the terms and conditions of the Creative Commons Attribution (CC BY) license (<https://creativecommons.org/licenses/by/4.0/>).

## 1. Introduction

Marine ferromanganese (Fe–Mn) nodules are typically formed through accumulation of colloidal precipitates of iron-manganese oxides (Mn oxides and Fe oxyhydroxides) on the seafloor of the world's oceans [1,2]. The Mn oxides and Fe oxyhydroxides are able to efficiently scavenge a large number of dissolved elements in ultra-trace concentrations from ocean water [3]. Due to their slow growth rate and continuous adsorption and co-precipitation with a wide range of metals, marine Fe–Mn nodules typically possess high concentrations of minor and trace elements, representing a resource for multiple critical elements (including Ni, Cu, Mn, Co, Mo, Ti, Li, and rare earth elements plus yttrium, or REE + Y) [1,3,4], which is a unique characteristic compared to terrestrial deposits.

The resource potential of Fe–Mn nodules is variable. Previous studies of Fe–Mn nodules showed that the enrichments of critical metals basically depend on the type of genetic process responsible for their growth [3,4]. In addition, water depth, bottom current strength, atmospheric inputs, surface productivity, bioturbation, sedimentation rate, benthic flux, topography, etc. determine their metal enrichment characteristics [5–10]. However, deciphering controls on chemical diversity in Fe–Mn nodules is a challenging undertaking,

as the enrichments are related to multiple environmental conditions simultaneously and many uncertainties remain about the geologic, chemical, and biological controls on fluxes of these metals into Fe–Mn nodules. Moreover, it is difficult to extrapolate from regional studies to global-scale phenomena.

Fe–Mn nodules from the Philippine Sea are distributively and compositionally different from other nodule fields from the global ocean. In general, nodules have a widespread occurrence on the seafloor, and hydrogenetic nodules are characterized by higher Co contents (~0.4 wt.%) [11,12]. Curiously, Fe–Mn nodules in the Philippine Sea have been found to widely form on topographic highs (e.g., seamounts and plateaus) rather than on the seafloor [8,13,14]. Previous studies have advanced our understanding of their formation and selective enrichment of metal elements. However, there are some issues and apparent inconsistencies with these nodules: the nodules are hydrogenetic but with low Co contents (<0.4 wt.%); Fe is correlated with Co, which is also abnormal as Co correlates to Mn in hydrogenetic nodules and crusts; and the presence of detrital minerals can have a dilution effect on Mn, Cu, and Co but cannot explain the high concentrations of Fe and REE + Y, etc. The discussion on these anomalies and the influence of the local oceanographic environment is very limited. Moreover, controls on chemical diversity and variability recorded in these ‘atypical hydrogenetic nodules’ have not been well documented yet.

Comprehensive and detailed studies on the Philippine Sea nodules have been lacking, but they are critical to more fully understand controls on critical metal enrichments in these nodules. Our investigation confirmed that Fe–Mn nodules were also densely distributed on the deep seafloor of both the West Philippine Basin and the East Philippine Basin. A set of nodules from twelve locations distributed on both sides of the Kyushu-Palau ridge at water depths of 4400–6000 m, including nodules near the topographic high and on the seafloor, were collected. To assess the enrichment and resource potential of critical metals in these Fe–Mn nodules, we conducted an investigation on their microstructures, bulk geochemistry, and in situ Fe–Mn oxyhydroxide geochemistry. We attempt to explain the controls of chemical variability and diversity recorded in these ‘atypical hydrogenetic Fe–Mn nodules’.

## 2. Materials and Methods

### 2.1. Sample Preparation

The nodules were collected from 4433 to 6017 m using the R/V *Hai Da Hao* in 2020 (Figure 1; Table S1 in the Supporting Materials). They occurred within the upper 2–3 cm of the sediments and were collected using box samplers. Fe–Mn layers of bulk nodule samples from 12 locations were ground to powder (<75 µm) after removing the debris cores for elemental composition analyses.

Four nodules (FND-11, FND-29, FND-31, and FND-49; Figure S1 in the Supporting Materials) were fully impregnated with epoxy resin under vacuum conditions and then cut into three pieces, with the cut direction vertical to the layers. One side of the middle parts was affixed to a micro slide using resin, and the other side of the middle parts was polished to produce a thin section 600 µm thick. The thin sections were then coated with a layer of carbon using a SC701C Quick Carbon Coater for the EPMA chemical analyses.

### 2.2. Analytical Methods

#### 2.2.1. XRF and ICP-MS Analyses

Major and trace elements were measured using X-ray Fluorescence (XRF) and inductively coupled plasma-mass spectrometry (ICP-MS) at Yanduzhongshi Geological Analysis Laboratories, Beijing, China, with a detection limit of ~0.01–0.1% and 0.01–0.1 µg/mL, respectively. To perform the major element analyses, 5 g of freeze-dried sample was formed into a pressed pellet for Axios XRF spectrometry after drying at 105 °C. Other trace elements were measured using ICP-MS after the dissolution procedure. An amount of 50 g of sample powder was digested with a mixture of ultrapure 3-acid digestion (HF, HNO<sub>3</sub>, and HCl) and heated at 190 °C for 48 h. The residuals were added to 1 mL HNO<sub>3</sub> and

evaporated again. Then, 4 mL of HNO<sub>3</sub> (20%) and 0.5 mL of Rh (μg/mL) internal standard solutions were added, and the mixture was dried until almost complete dryness (150 °C for 12 h). After cooling and adding hydrogen peroxide, the samples were moved to disposable plastic bottles containing 2% HNO<sub>3</sub>, diluted 2000×, and analyzed using ICP-MS.

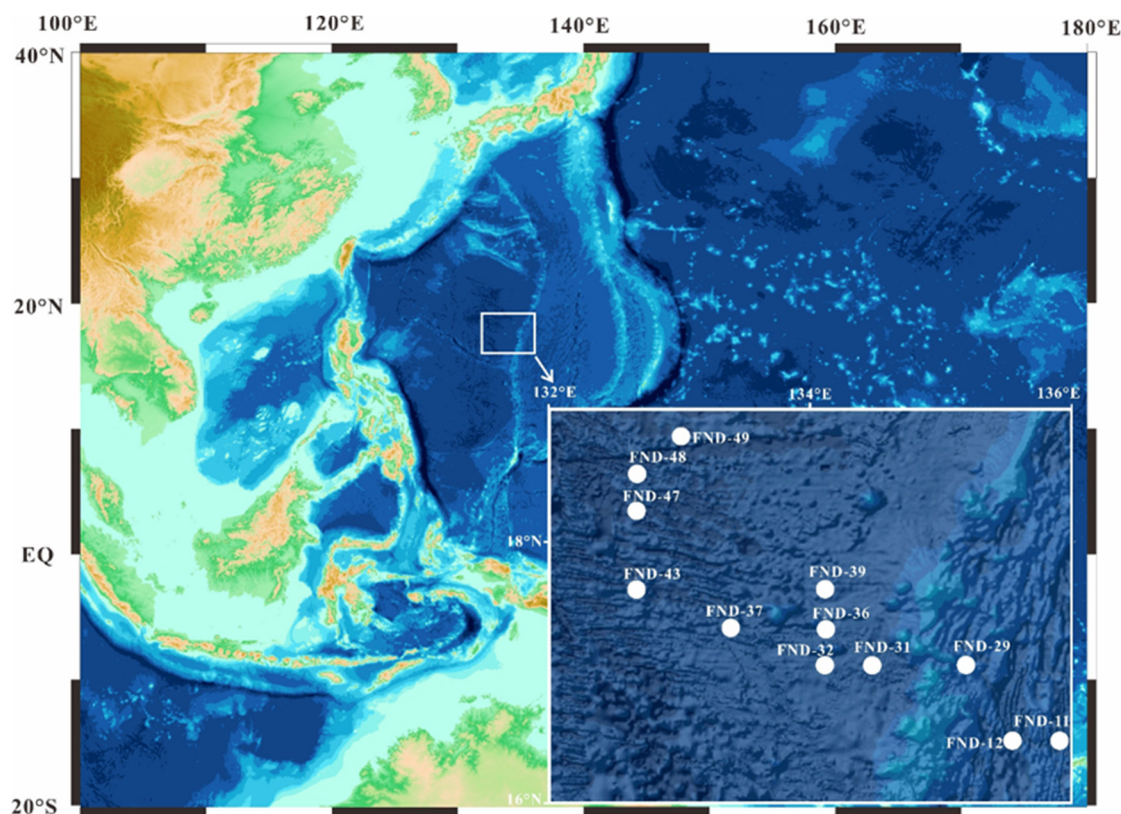


**Figure 1.** Sample sites of Fe–Mn nodules in this study.

### 2.2.2. BSE Images

BSE images of the samples were taken by using an 8230 EMPA (JEOL Corporation, Tokyo, Japan) at the Hebei Key Laboratory of Earthquake Dynamics, Sanhe, China.

### 2.2.3. EMPA Spot Analysis

After microstructure observations through BSE images, FND-31 and FND-49 were chosen for in situ analyses (EMPA and LA-ICP-MS) as they presented more sublayer types than other nodules, and they also were the representatives of shallow and deep water nodules, respectively (Figure 1). The EPMA results of FND-49 have been reported in our previous study [15].

Ti, K, Ca, Pb, Na, Mg, Al, P, Si, Fe, Co, Mn, Ni, and Cu were determined on positions where Fe–Mn oxides were dense and the surface flat using a 8230 EMPA (JEOL Corporation, Japan) at the Hebei Key Laboratory of Earthquake Dynamics, Sanhe, China. The individual Fe–Mn oxides were measured with a focused 1 μm beam, and the counting times were 10 s for Si, Na, Mg, Ni, Cu, Mn, Ca, Al, K, Fe, Ti, and P; 50 s for Co; and 45 s for Pb. Haematite (Fe), rhodochrosite (Mn), synthetic Ni<sub>2</sub>Si (Ni), cobaltite (Co), apatite (Ca, P), albite (Na), kaersutite (Mg, Al, Si), biotite (K), cuprite (Cu), krokoite (Pb), and rutile (Ti) were used as standards (SPI).

### 2.2.4. In Situ LA-ICP-MS Analysis

In situ trace element analysis was performed at the Tuoyan in situ Analysis Lab, Guangzhou, China, using a 193-nm ArF excimer laser system coupled with an Agilent

7900 Quadrupole ICP-MS instrument. A laser spot size of 30  $\mu\text{m}$  in diameter was used with an energy density of 3.5  $\text{J}/\text{cm}^2$ . Laser repetition rate was 6 Hz. Each analysis consisted of 40 s of background measurement and 45 s of data acquisition. External calibration was performed using BHVO-2G, NIST610, and NIST612. Details of the data calculations are described in [16,17].

### 3. Results

#### 3.1. Bulk Nodules

Table 1 lists the major and trace element compositions of the bulk nodules. The nodules displayed high contents of Mn (12.89–21.8 wt.%), Fe (13.48–21.81 wt.%),  $\text{SiO}_2$  (17.21–28.70 wt.%), and  $\text{Al}_2\text{O}_3$  (5.37–8.26 wt.%). Mn/Fe ratios varied from 0.74 to 1.40, with an average of 1.06. Compared to typical hydrogenetic nodules found in the Cook Islands, the nodules in our study displayed relatively higher contents of Fe and REY and lower contents of Co.

**Table 1.** Element contents of bulk nodules (normalized to 0%  $\text{H}_2\text{O}$ ). LOI = Loss on Ignition.

Samples	FND-11	FND-12	FND-29	FND-31	FND-32	FND-36	FND-37	FND-39	FND-43	FND-47	FND-48	FND-49
$\text{SiO}_2$ (%)	19.48	24.72	28.7	20.01	20.04	19.78	17.21	18.88	18.59	20.18	19.59	19.18
$\text{Al}_2\text{O}_3$	6.12	7.78	8.26	5.96	5.42	5.46	5.51	5.37	5.79	6.11	6.07	5.83
CaO	2.6	2.18	2.31	2.32	2.22	2.2	2.36	2.21	2.32	2.21	2.18	2.22
MgO	2.41	2.79	2.23	2.32	2.15	2.1	2.31	2.28	2.49	2.46	2.71	2.73
$\text{K}_2\text{O}$	0.83	1.34	1.61	0.88	0.78	0.77	0.73	0.78	0.8	0.91	0.88	0.9
$\text{Na}_2\text{O}$	2.27	2.92	2.65	2.27	2.16	2.17	2.14	2.25	2.23	2.5	2.26	2.36
$\text{TiO}_2$	1.55	0.96	1.39	1.55	1.56	1.69	1.54	1.35	1.42	1.1	1.07	1.04
$\text{P}_2\text{O}_5$	0.65	0.51	0.65	0.68	0.72	0.74	0.71	0.66	0.65	0.6	0.59	0.58
MnO	24.21	24.35	16.64	22.74	21.94	20.84	25.22	25.15	25.94	26.58	27.28	28.15
$\text{TFe}_2\text{O}_3$	26.12	19.27	24.39	27.17	29.58	31.18	28.22	26.69	26.04	23.26	23.23	22.55
LOI	13.32	12.8	11.73	13.67	13.52	13.44	14.19	14.13	14.01	14.32	13.98	14.31
Li (ppm)	60.3	142	26.6	44.9	43	29.6	56.2	68.5	68.1	103	96.9	120
Cu	2497	3657	1351	2544	2124	2073	2354	2701	2837	3359	3989	3792
Co	2469	1624	2045	2337	2402	2338	2494	2216	2405	1826	1919	1919
Ni	4048	5057	2447	4011	3396	2950	4204	4329	4873	5168	6193	6199
La	193	138	168	183	190	190	196	190	178	157	154	160
Ce	736	474	713	885	988	1024	968	893	857	703	648	654
Pr	43.7	31.4	40.6	42	44	43.8	43.8	43.2	40.3	36.6	35.9	34.7
Nd	185	126	165	181	192	190	189	188	172	152	149	146
Sm	39.9	28.4	36.3	40.2	43	43.5	42.2	42.4	38.7	34.7	34.1	33.3
Eu	10.1	7.16	9.04	10.1	10.6	10.6	10.6	10.6	9.6	8.68	8.52	8.29
Gd	45.3	31.6	40.1	46	48.5	48.8	48.6	48.2	44.5	39.4	38.2	37.5
Tb	6.96	4.81	5.97	6.91	7.17	7.19	7.32	7.22	6.74	6.06	5.88	5.8
Dy	39.7	27.6	33.1	39.4	40.6	40.4	41.5	40.5	38.3	35	33.9	33.4
Ho	8.09	5.59	6.6	7.96	8.14	7.97	8.44	8.23	7.86	7.16	6.84	6.88
Er	22.1	15.1	17.8	21.3	21.6	21.3	22.8	22.1	21.2	19.2	18.5	18.4
Tm	3.14	2.17	2.48	3.11	3.11	3.04	3.3	3.14	3.06	2.79	2.68	2.65
Yb	20.8	14.2	16.3	20.6	20.4	20.1	21.7	20.7	20.4	18.2	17.5	17.4
Lu	3.12	2.12	2.4	3.06	3.06	3.06	3.29	3.14	3.11	2.78	2.67	2.68
Y	144	103	127	134	132	130	142	137	134	124	118	119
$\Sigma\text{REE}$	1356.9	908.2	1256.7	1489.6	1620.2	1653.8	1606.6	1520.4	1440.8	1222.6	1155.7	1161.0
$\text{Eu}_{\text{SN}}/\text{Eu}^*_{\text{SN}}$	1.11	1.11	1.11	1.09	1.08	1.07	1.09	1.09	1.08	1.09	1.1	1.09
$\text{Ce}_{\text{SN}}/\text{Ce}^*_{\text{SN}}$	1.9	1.71	2.05	2.39	2.56	2.66	2.47	2.34	2.4	2.2	2.07	2.08

1.  $\Sigma\text{REE}$  = sum of rare earth elements. 2.  $\text{Eu}_{\text{SN}}/\text{Eu}^*_{\text{SN}}$  is Eu anomaly normalized to PAAS values.  $\text{Eu}_{\text{SN}}/\text{Eu}^*_{\text{SN}} = 2 \times \text{Eu}_{\text{SN}}/(\text{Sm}_{\text{SN}} + \text{Gd}_{\text{SN}})$ . 3.  $\text{Ce}_{\text{SN}}/\text{Ce}^*_{\text{SN}}$  is Ce anomaly normalized to PAAS values.  $\text{Ce}_{\text{SN}}/\text{Ce}^*_{\text{SN}} = 2 \times \text{Ce}_{\text{SN}}/(\text{La}_{\text{SN}} + \text{Pr}_{\text{SN}})$ .

The REE contents were high, ranging from 1011 to 1783 ppm (mean 1495 ppm), with Ce displaying the highest contents (474–1024 ppm) (Table 1). The nodules exhibited high Nd contents (126–192 ppm), low  $(\text{Y}/\text{Ho})_{\text{SN}}$  ratios (1.71–2.66) (normalized to Post Archaean Australian shale, PAAS) [18], and positive Ce anomalies ( $\text{Ce}_{\text{SN}}/\text{Ce}_{\text{SN}} = 1.71$ –2.66), showing the same characteristics with hydrogenetic nodules and crusts [1,2,19,20]. Additionally, the nodules displayed weakly positive Eu anomalies ( $\text{Eu}_{\text{SN}}/\text{Eu}_{\text{SN}} = 1.07$ –1.11), which excludes hydrothermal processes and suggests an oxidizing environment [8,20,21].

#### 3.2. Chemical Variation in Sublayers (EPMA and LA-ICP-MS Spot Analysis)

BSE images of the nodules show that they exhibit complex internal structures (Figure 2). These layers vary in chemistry, continuity, and reflectivity. The major and trace element

contents of these layers obtained from EPMA and LA-ICP-MS analyses are showed in Tables 2 and S2.

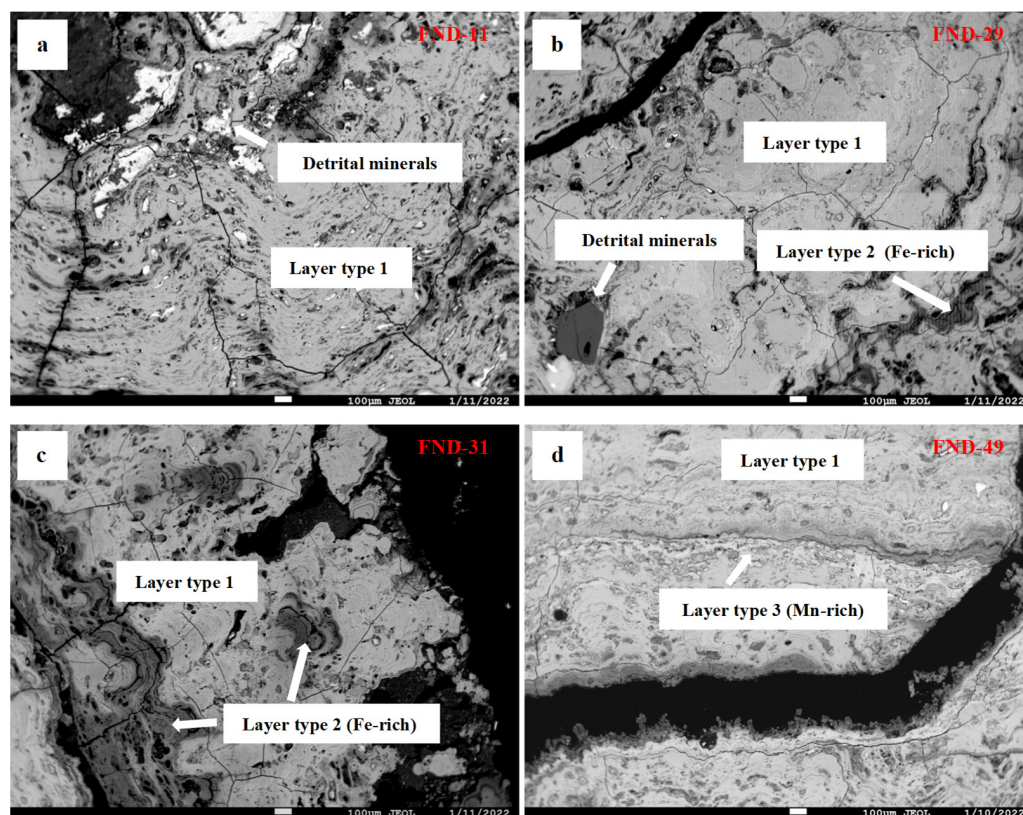


Figure 2. (a–d): BSE images of three layer types of nodules from the Philippine Sea.

Table 2. Average element content of individual layers (EMPA data; wt.%).

Element	Layer Type 1				Layer Type 2				Layer Type 3			
	Average	Max	Min	STD.DEV	Average	Max	Min	STD.DEV	Average	Max	Min	STD.DEV
K	0.36	0.82	0.21	0.12	0.24	0.33	0.19	0.06	0.50	0.74	0.17	0.24
Ti	1.03	1.63	0.58	0.25	1.33	1.65	1.08	0.21	0.21	0.58	0.05	0.22
Ca	2.30	2.70	1.45	0.26	0.92	1.15	0.67	0.20	1.42	2.20	0.97	0.52
P	0.37	0.47	0.18	0.06	0.33	0.41	0.24	0.06	0.08	0.17	0.03	0.05
Pb	0.18	0.27	0.05	0.06	0.19	0.28	0.14	0.06	0.04	0.08	0.00	0.03
Na	0.61	1.56	0.30	0.24	0.55	0.65	0.40	0.10	0.92	1.32	0.52	0.37
Mg	1.02	2.31	0.57	0.32	0.65	0.72	0.60	0.06	3.65	3.80	3.35	0.18
Al	2.09	3.89	1.41	0.42	1.50	1.76	1.32	0.16	2.88	4.70	2.10	1.04
Si	4.98	10.37	3.10	1.34	4.74	6.37	3.30	1.10	2.53	3.69	1.31	1.02
Mn	22.67	30.09	12.65	3.44	8.68	13.37	6.03	3.24	35.82	39.47	28.35	4.58
Fe	22.42	29.06	15.72	3.10	24.66	29.76	18.82	4.55	3.60	7.11	0.82	2.39
Co	0.46	0.83	0.15	0.14	0.28	0.50	0.16	0.14	0.16	0.26	0.04	0.08
Ni	0.32	1.16	0.11	0.23	0.06	0.14	0.01	0.05	2.29	2.83	1.83	0.45
Cu	0.18	0.60	0.04	0.12	0.08	0.14	0.03	0.04	0.85	0.90	0.71	0.08
Mn/Fe	1.05	1.91	0.44	0.29	0.37	0.62	0.22	0.16	17.29	46.37	4.86	16.92
Ni + Cu	0.50	1.76	0.21	0.34	0.15	0.28	0.07	0.08	3.14	3.72	2.69	0.47

### 3.2.1. Layer Type 1 (Normal Mn/Fe Ratio)

Layer type 1 is the predominant layer observed in the nodules, displaying a dense, mottled growth structure and some with a column structure, which are typical for hydroge- netic crusts. The Mn/Fe ratios are between 0.44–1.91 (Table 2). The Ni + Cu concentrations range between 0.21 and 1.76 wt.%, and the Co concentrations range from 0.15 to 0.83. The compositions of Layer type 1 are generally the same trend as that of the bulk nodules.

Table S2 shows REE statistics for sublayers. Layer type 1 exhibited a high REE content of 2647–3236 ppm, especially for Ce (1484–1719 ppm), and positive Ce anomaly ( $Ce_{SN}/Ce^*_{SN} = 2.15\text{--}2.75$ ) and weakly positive Eu anomalies ( $Eu_{SN}/Eu^*_{SN} = 1.07\text{--}1.16$ ).

### 3.2.2. Layer Type 2 (Fe-Rich; Low Mn/Fe Ratio)

Layer type 2 exhibits a mottled porous growth structure with low reflectivity. The Mn/Fe ratios are between 0.22 and 0.62 (Table 2). Ni + Cu concentrations range from 0.07 to 0.28 wt.%, and Co concentrations are between 0.16 and 0.50 wt.%. The REE contents show almost the same characteristics as Layer type 1 (Table S2).

### 3.2.3. Layer Type 3 (Mn-Rich; High Mn/Fe Ratio)

Layer type 3 exhibits fine and dense growth structures (0.01 to 0.05 mm thick) with high reflectivity. This type of layer is relatively uncommon and occurs as lamina within Layer type 1. The boundaries between the different layers are clearly defined. Layer type 3 is characterized by high Mn concentrations relative to Fe, exhibiting extremely high Mn/Fe ratios (4.86–46.37), and high contents of Ni (1.83–2.83 wt.%) and Cu (0.71–0.90 wt.%), but low Co (0.04–0.26 wt.%) contents (Table 2).

Layer type 3 exhibited a low REE content of 693–701 ppm, weakly positive Eu anomaly ( $Eu_{SN}/Eu^*_{SN} = 1.07\text{--}1.14$ ), and relatively weak positive Ce anomaly ( $Ce_{SN}/Ce^*_{SN} = 1.60\text{--}1.63$ ) (Table S2).

## 4. Discussion

### 4.1. Controls of the Different Genetic Processes

The nodules were formed mainly through hydrogenetic processes, as indicated by microstructural and bulk geochemistry. They exhibit mottled structure (Layer type 1; Figure 2), which is similar to typical hydrogenetic nodules and crusts [19,22]. The bulk geochemical studies showed low Mn/Fe ratios (0.7–1.4) and high REE contents (908–1653, average 1366 ppm) (Table 1), which is also consistent with the composition of typical hydrogenetic nodules and crusts [19,22] and is significantly different from the composition of hydrogenetic-diagenetic nodules from the Clarion and Clipperton Zone (Mn/Fe = 4.6,  $\Sigma REE = 707$  ppm) and diagenetic nodules from the Peru Basin (Mn/Fe = 5.6,  $\Sigma REE = 334$  ppm) [12,23]. Moreover, on the basis of Fe–Mn–(Cu + Ni + Co)  $\times 10$  and  $15 \times (Cu + Ni) - 100 \times (Zr + Y + Ce) - (Fe + Mn)/4$  ternary diagrams (Figure 3a,b), which classify the nodules as hydrogenetic, diagenetic, and hydrothermal [24,25], shallower-water nodules mostly are of hydrogenetic type. However, deep-water nodules exhibit relatively more complicated behavior, with higher Cu + Ni contents and a continuum towards oxic diagenetic field (Figure 3b, blue dotted arrow). Overall, deep-water nodules are still mostly characterized by hydrogenic origin as evident in the REE + Y plots. On the basis of discrimination diagrams proposed by Bau et al. (2014) [26], the nodules fall within the hydrogenetic area (Figure 3c,d). These nodules have positive Ce anomalies and a high Nd content (126–192 mg kg<sup>−1</sup>), showing that nodules are mostly hydrogenetic nodules (Table 1).

The use of high-resolution EMPA and LA-ICP-MS analyses enables the identification of microlaminations associated with various genetic processes. These high-resolution analyses reveal a wider dispersion of genetic processes. Deep-water nodule FND-49 contains fine veins (Layer type 3; Figure 2d) with high reflectivity, which exhibit extreme Mn/Fe ratios (4.86–46.37) and high Ni (18,280–28,270 ppm) and Cu (7100–8970 ppm) contents but low Co contents (380–2620 ppm). These characteristics are similar to diagenetic nodules found in the Clarion–Clipperton zone and the Peru Basin [12,23]. The geochemistry of the Mn-rich layers suggests that they are of diagenetic origin, falling mostly within the diagenetic field in the Fe–Mn–(Cu + Ni + Co)  $\times 10$  ternary diagram (Figure 3a). The existence of these diagenetic layers indicates that deep-water nodules were affected by diagenetic processes, which differs significantly from the layers found in shallow-water nodules. As a result of these diagenetic layers, deep-water nodules exhibit a continuum towards the

oxic diagenetic field (Figure 3b). Additionally, LA-ICP-MS analyses revealed weak positive Ce anomalies in these layers ( $Ce_{SN}/Ce^*_{SN} = 1.6\text{--}1.63$ ; Table S2), which suggest that the diagenetic redox conditions were early oxic diagenesis. This diagenetic process likely occurred under oxic conditions in the pore water, similar to hydrogenic processes observed through X-ray photoelectron spectroscopy measurements of nanometer-thin surface layers of nodules in contact with oxic pore water [27].

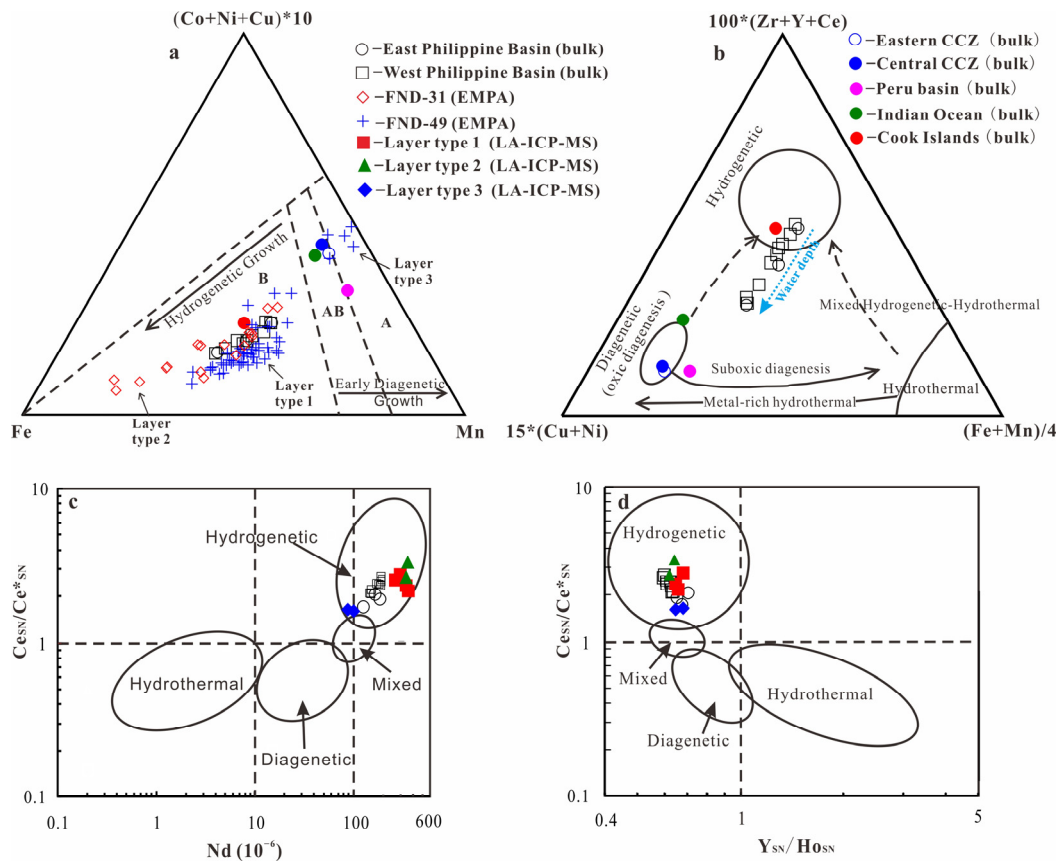


**Figure 3.** (a) Fe–Mn–(Cu + Ni + Co)  $\times$  10 diagram for genesis of Fe–Mn deposits from [24]. A: diagenetic, B: hydrogenetic, and AB: mixed type; (b)  $15 \times (Cu + Ni) - 100 \times (Zr + Y + Ce) - (Fe + Mn)/4$  discrimination diagram for genesis of Fe–Mn deposits from [25]; (c,d) Discrimination diagrams based on geochemical relationships from [26]. Other data from the Clarion–Clipperton zone (CCZ), Peru Basin, Indian Ocean, and Cook Islands are from [1,19].

In contrast, Layer type 2 with low reflectivity detected within shallower-water nodules FND-29 and FND-31 shows characteristics of high Fe content and positive Ce anomaly but low Cu and Ni content (Figure 4a–c; Table S2). The element characteristics suggest that the Fe-rich layers are derived from hydrogenetic processes. The Fe–Mn–(Cu + Ni + Co)  $\times$  10 diagram and REE + Y plots also confirm that these layers are of hydrogenetic origin (Figure 3a).

As a result, the chemical composition of nodules is controlled by the formation processes of nodules: hydrogenetic or diagenetic. Generally, diagenetic precipitation is enriched in Mn, Cu, and Ni but depleted in Fe, Co, and REE + Y [1,2,12,28–31], while hydrogenetic nodules are highly enriched in Co and REE + Y [28,29,32,33]. However, it should be noted that these element composition characteristics and classification schemes are specific to the environment and cannot be applied universally to all types of Fe–Mn deposits. Several distinguishing characteristics make the Philippine Sea nodules different from those nodules in other regions of the global ocean, and what controlled the nodule formation processes still needs more discussion, as seen below.

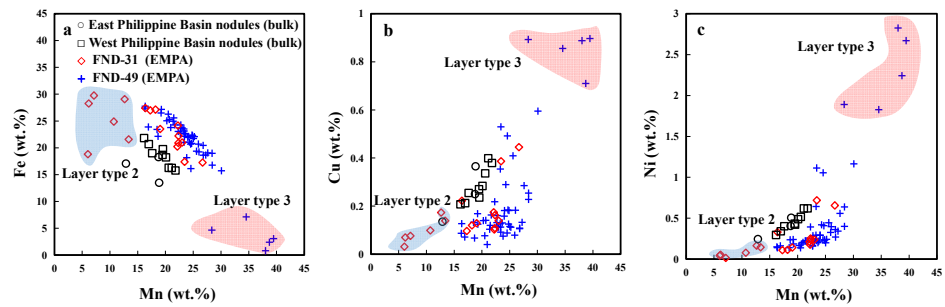


**Figure 4.** (a–c): Relationships of Mn with Fe, Ni, and Cu in the nodules.

4.2. Effect of Water Depth: CCD and Diagenetic Origin

The fact that metal contents in hydrogenetic crusts vary with depth was already discussed in previous publications [34–36]. However, the discussion about the effect of water depth on Fe–Mn nodules is very limited. Here, we observe metal concentration variations of nodules in the Philippine Sea with water depth (Figure 5).

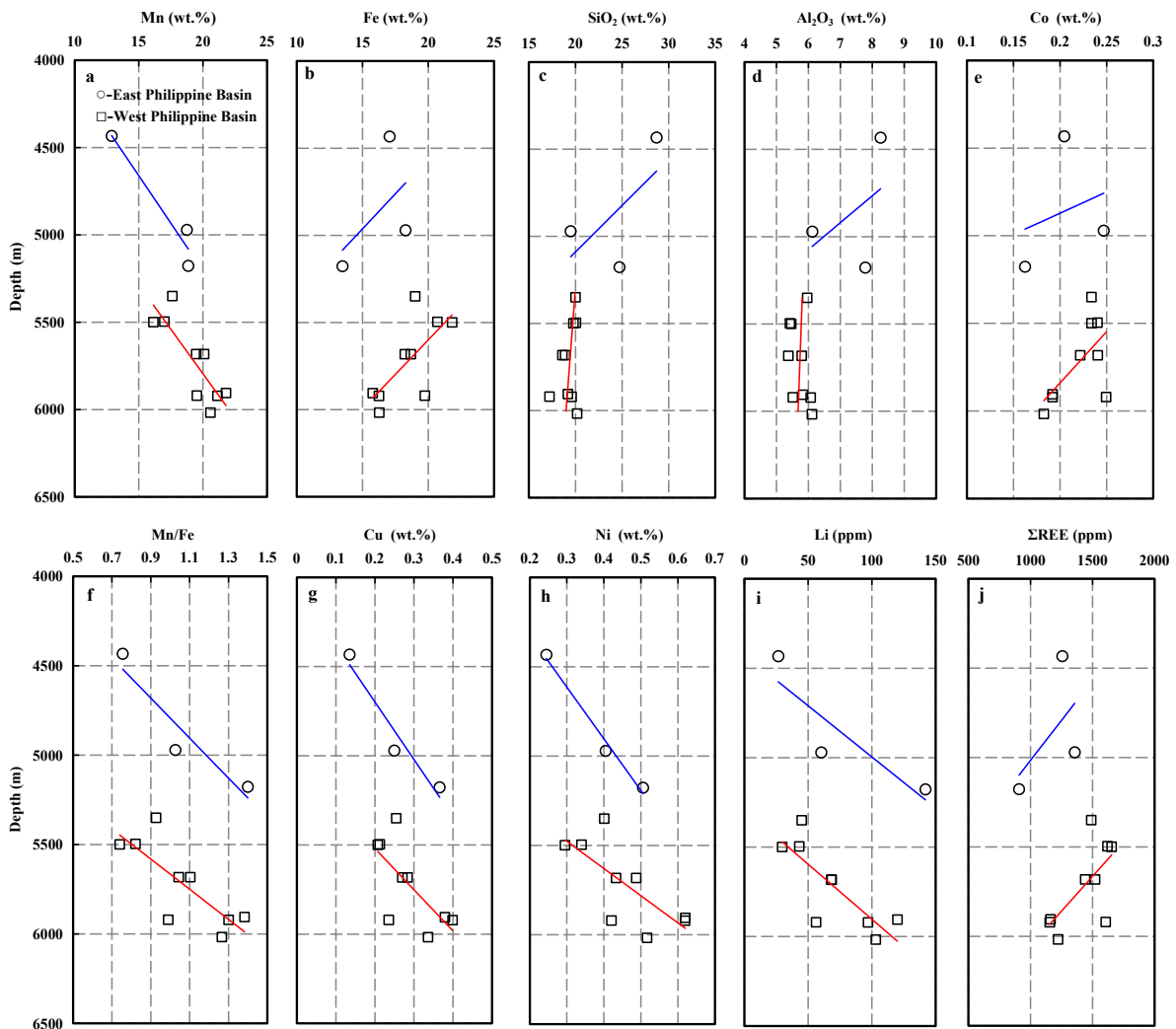


**Figure 5.** (a–j): plots of elements (Mn, Fe, SiO<sub>2</sub>, Al<sub>2</sub>O<sub>3</sub>, Co, Mn/Fe, Cu, Ni, Li, and ΣREE; from bulk analyses) concentrations of samples from the Philippine Sea versus the water depths ( $n = 12$ ; Table 1). Blue lines show linear regressions of the East Philippine Sea nodules, while red lines show linear regressions of the West Philippine Sea nodules.

For crusts found on seamounts located above the carbonate compensation depth (CCD), two sources are presumed to provide the necessary Mn and Fe for the growth of hydrogenetic crusts: (1) Mn ( $\text{Mn}^{2+}$ ) is believed to be sourced from the oxygen-minimum zone (which has not yet undergone oxidation), and (2) Fe-oxyhydroxide is released during the dissolution of carbonate plankton such as calcite skeletons and aragonite [34–36]. The concentration of Mn in crusts decreases with increasing water depth since the main Mn source is the oxygen-minimum zone, while an increase of released Fe-oxyhydroxide particles near the CCD causes Fe enrichment and Mn dilution.

The water depth ranges of our sample sites (~4400–6000 m) are generally below the CCD. In contrast with the case of hydrogenetic crusts above CCD, Mn content rises, and the Fe content drops in the nodules as the water depth increases (Figure 5a,b). The Mn/Fe ratio increases from 0.7 at shallower depths to 1.4 in basin regions (Figure 5f). Similar to the crusts near CCD, the high Fe contents in the shallower-water nodules might depend on the release of Fe oxyhydroxide from CCD. The high calcite dissolution rate contributes to the budget of Fe phases available for the hydrogenetic growth of the shallower-water nodules, and the high supply of Fe phases might have a diluting effect on Mn Cu and Ni (Figure 5a,g,h).

The high Mn content of seafloor nodules can be explained by Mn having another source. Mn-rich layers identified in FND-49 (~6000 m), with a clear diagenetic origin, yielded low contents of Co and high contents of Ni and Cu. The influence of these diagenetic layers on the bulk geochemistry might explain the low Co, REE contents and high Ni, Cu contents in these deep-water nodules (Figure 5e,g,h,j). The higher Ni, Cu, and Mn of deep-water nodules might be caused by oxidation of organic matter in deep-ocean sediments, resulting in the reduction and dissolution of Mn oxides and release of associated elements (Ni, Cu, among others) [2,37].

In addition, high Li concentrations in deep-water nodules (Figure 5i) also indicate a diagenetic origin, as the concentration of Li tends to increase with the diagenetic component [38]. Diagenetic processes lead to the reduction and dissolution of Mn oxides and the release of Li [2,37]. Typical hydrogenetic nodules and crusts from the Cook Islands and northwest Pacific exhibit low Li concentrations ranging from approximately 5.4–41 ppm and 3.0–3.7, respectively [19,36]. Hydrogenetic-diagenetic nodules from the Clarion–Clipperton zone display an average Li concentration of ~130 ppm, whereas diagenetic nodules from the Peru Basin have an average Li content of about 310 ppm [39]. The Li contents of the deep-water nodules in our study range from 97–142 ppm, which is similar to that of the hydrogenetic-diagenetic nodules from the Clarion–Clipperton zone. The high Cu, Ni, and Li contents in the nodules result from the diagenetic input [32,38]. Thus, although these nodules mostly show the characteristics of hydrogenetic precipitation (Layer type 1), their higher Mn, Ni, Cu, and Li contents indicate that they are affected by diagenetic processes within the underlying sediments.

Thus, for the Philippine Sea nodules under the CCD, two sources are assumed in order to supply the growth of these nodules: (1) diagenetic Mn from deep-sea basins and (2) Fe oxyhydroxide released from carbonate plankton dissolution. With increasing water depth, the Mn concentrations of nodules increase, and a high supply of Fe-oxyhydroxide particles near the CCD cause an enrichment of the Fe and a dilution of the Mn.

In addition, BSE images show that detrital minerals are relatively more abundant in East Philippine Basin nodules (FND-11 and FND-29; Figure 2a,b). The presence of alumina-silicate detrital minerals in East Philippine Basin nodules is also evidenced by bulk analyses:  $\text{SiO}_2$  and  $\text{Al}_2\text{O}_3$  contents of East Philippine Basin nodules are higher than that of West Philippine Basin nodules (Figure 5c,d). The presence of detrital minerals in East Philippine Basin nodules promotes a higher dilution effect of detrital contents on East Philippine Basin nodules.

#### 4.3. The ‘Co Problem’: Co–Fe Correlation and Low Co Content

These ‘atypical hydrogenetic Fe–Mn nodules’ are hydrogenetic but with lower Co contents (0.16–0.25, average 0.22; <0.4 wt.%). Moreover, a different relationship of Co to the Mn and Fe has been observed: bulk metal contents show that Co has a stronger correlation with Fe than Mn (Figure 6a), which is also anomalous as Co shows a positive relationship with Mn in hydrogenetic nodules and crusts [19,36]. It looks as if Fe phases may play a more important role than Mn minerals in scavenging Co during nodule formation in the Philippine Sea. However, previous studies all suggest Co are absorbed by the Mn mineral phases, e.g. [40,41]. These anomalies of Co have been also found in nodules from other areas of the Philippine Sea [8,14], but the cause of these anomalies has not been well documented yet. To gain further insight, we conducted in situ EMPA tests on Fe–Mn oxyhydroxide of the samples (FND-31 and FND-49).

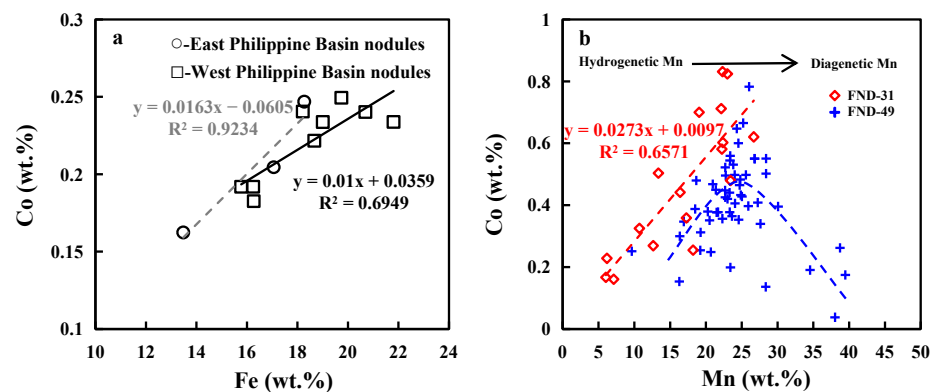


**Figure 6.** (a): Relationship of Fe with Co (from bulk analyses); (b): Relationship of Mn with Co (from in situ EMPA analyses).

Our results show that Co is positively related to Mn content in hydrogenetic layers (normal layers and Fe-rich layers), while anticorrelated with Mn in diagenetic layers (Mn-rich layers) (Figure 6b). This difference between Co precipitation should be controlled by the special processes of Co absorption. We found Co content is determined by two variables: Mn and growth rate. Co exists in seawater mainly as a hydrated divalent cation and is adsorbed by hydrous  $\text{MnO}_2$  colloids combined with an oxidation to  $\text{Co}^{3+}$  after outer sphere adsorption [35]. As Co is adsorbed at the surfaces of  $\text{MnO}_2$  colloids, the amount of Mn oxide precipitated on nodule surface would represent the Co adsorption ability. Indeed, Co is positively related to Mn content in ‘pure hydrogenetic crusts’ above the CCD, in which the growth rate is typically slow [42]. However, Co is inversely proportional to Mn in diagenetic layers (high growth rates). Co is considered to be an element most characteristic of hydrogenetic precipitation in crusts and nodules and is assumed to have a constant flux in the water column, regardless of the water depth [43]. As a result, diagenetic Mn (pore water) and hydrogenetic Co (seawater) definitely behave differently: the diagenetic Mn would increase the nodule growth, and Mn-flux is proportional to the growth rate, in contrast to the Co-flux, which appears to be constant over the growth rate. This suggests that the Co-enrichment in diagenetic Mn phases should be inversely related to the growth rate: the slower the growth rate the higher the Co concentration. As discussed in the previous section, Mn-rich layers, identified in deep-water nodules (FND-49) with a clear diagenetic origin, and the higher Mn/Fe ratios (~1.3) of nodules in basin regions indicate that nodules in sedimentary deep-sea basins have a diagenetic Mn origin. Thus, the low Co content in the Mn-rich, deep-water nodules can be attributed to a higher growth rate caused by diagenetic Mn origin from pore water in the sediments. The positive Co–Fe correlation of bulk analyses is caused by two anticorrelations: Co and Fe are both anticorrelation with diagenetic Mn. As a result, Figure 6a is misleading about the nature of the Co-host phase. Moreover, when Mn contents are similar, Co contents of FND-49 (~6000m) are mostly

much smaller than that of FND-31 (~5350m) (Figure 6b), which also indicates FND-49 has a higher growth rate influenced by the diagenetic Mn origin.

Although the Co content (~0.25 wt.%) of shallower-water nodules is higher than that of deep-water nodules (Figure 5e), it is still lower than that of typical hydrogenetic nodules and crusts (>0.4 wt.%) [19,22]. The shallower-water nodules do not show any diagenetic overprint. The low Co contents of the shallower-water nodules can be ascribed to the Fe origin from CCD. As described above, Fe precipitation would have a diluting effect on Co since Mn minerals are the carrier phases for Co. The high Fe content and low Co content of shallower-water nodules are similar to the characteristic of hydrogenetic crust found near CCD (Co= ~0.28 wt.%) [42].

#### 4.4. The Conundrum of REE Incorporation in the Nodules

The absorption of REE between Mn and Fe phases is still under discussion. There is a lack of information regarding the location of REE within the mineral structure of these nodules [44]. Previous studies have suggested several factors that affect the scavenging of REE between the Mn and Fe phases, and different conclusions have been made: (1) the slightly positively charged FeOOH particles can adsorb ions that form anionic complexes such as carbonate ( $\text{REE}(\text{CO}_3)^{2-}$ ) [33,45,46]; (2) the Mn-phase prefers to collect light rare earth elements (LREE) as LREE form monocarbonate complexes ( $\text{REECO}_3^+(\text{aq})$ ), while the Fe-phase (in contrast) prefers heavy rare earth elements (HREE) as HREE form bicarbonate complexes ( $\text{REE}(\text{CO}_3)^{2-}$ ) [42]; and (3) the significant positive correlation of REE with Fe is attributed to their similar supply mechanism and not due to the incorporation of REE in the Fe phase [44].

The PAAS normalized REE and Y concentrations of bulk nodules exhibit similar distribution patterns to those of deep-sea Fe–Mn hydrogenetic nodules, with a positive Ce anomaly and negative Y anomaly (Figure 7a). Similar to Co, bulk analyses show REE has a stronger correlation with Fe than Mn (Figure 7b). However, as described above, the Co–Fe correlation is misleading about the nature of the Co-host phase: the Co–Fe correlation of bulk analyses is actually caused by the growth rate. It suggests that simple statistical interelement correlations of bulk geochemical analyses cannot be used to assess the association of metals in the mineral phases of nodules. Thus, whether Fe phases may play a more important role than Mn minerals in scavenging REE + Y needs more evidence. In order to gain further insight and compare the behavior of REE, we conducted in situ LA-ICP-MS tests on Fe–Mn oxyhydroxide of different genetics. We plotted the contents of REE + Y for each of the sublayers normalized to PAAS (Figure 8a).

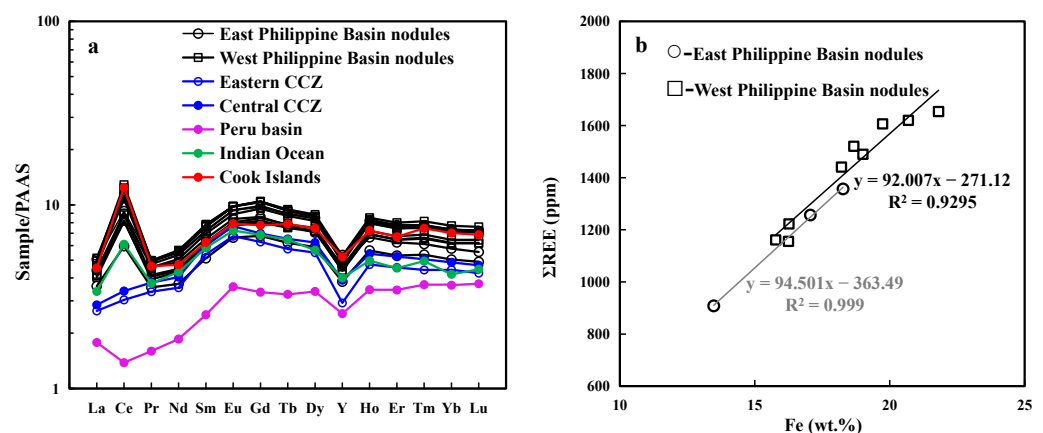


**Figure 7.** (a) PAAS [18] normalized REE + Y of bulk nodules (ICP-MS). Other data are taken from [1,19]; (b) Relationship of Fe with REE (from bulk analyses). REY of bulk (continuous lines) and spot LA-ICP-MS analysis.

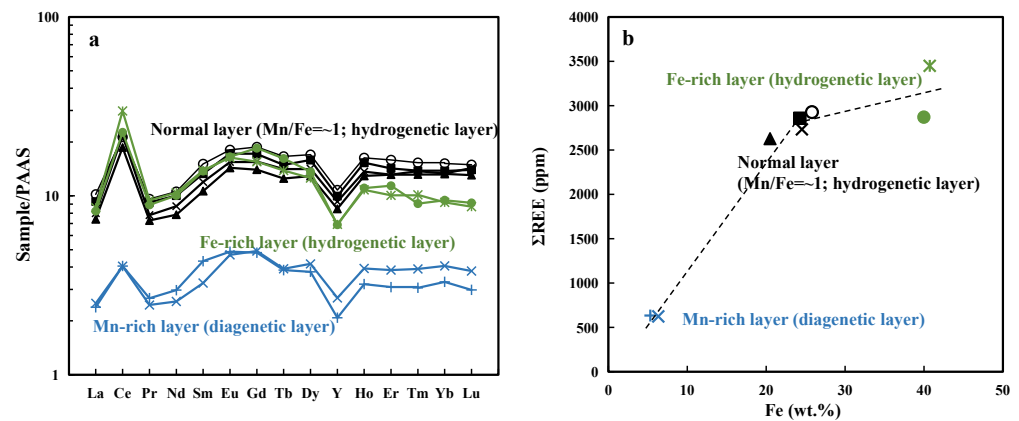


**Figure 8.** (a) PAAS [18] normalized REE + Y of each sublayer (LA-ICP-MS); (b) Relationship of Fe with REE (from in-situ LA-ICP-MS analyses).

When classified according to subtype layers, hydrogenetic layers (Fe-rich layers and normal layers) showed much higher REE + Y contents than that of diagenetic type layers (Mn-rich layers) (Figure 8a). However, for hydrogenetic layers, Fe-rich layers and normal layers had similar average REE + Y concentrations. REE contents do not show positive relationship with Fe in hydrogenetic layers (Figure 8b). These distributions of REE contents in different sublayers show a meaningful difference. If the REE substitutes into the Fe phase, the Fe-rich layers in the nodule would have a higher REE content than the normal layers, but Fe-rich layers did not display a higher REE distribution pattern (Figure 8a,b).

A recent sequential leaching experiment on hydrogenetic crusts revealed that REE enter both Fe phases and Mn phases [4]. Our results suggest that the significant positive correlation of REE with Fe is not due to the incorporation of REE into Fe-oxyhydroxide phase and might be ascribed to growth rate of nodules, which was also proposed by [47]. This suggests that lower growth rates lead to higher REE concentrations. Consistent with this interpretation, the growth rate of Fe–Mn oxides increases in the order hydrogenetic < diagenetic < hydrothermal oxides [40], while the REE content decreases in the reverse order.

Additional evidence for the inference is the Ce anomaly. Most REE are trivalent ions that are nonredox sensitive and have similar chemical reactivity, and the adsorption of these elements occurs over similar time scales [47]. However,  $Ce^{3+}$  has a different property as it would be oxidized to  $Ce^{4+}$  after the adsorption [40,47,48]. Ce and Co are both oxidized by Mn oxides, but while Ce could be oxidized also by Fe oxyhydroxides, Co is not, e.g. [40,49]. Thus, Co is positively related to Mn content in ‘pure hydrogenetic layers’ when the growth rates are low (Figure 6b), while Ce shows similar contents in ‘pure hydrogenetic layers’, no matter whether in Fe-rich layers or normal layers (Figure 8a). In addition, Ce anomalies are weak, and Ce contents are low in Mn-rich layers (high growth rate; Figure 8a; Table S2). It is also consistent with the observations and results of XANES and EXAFS and chemical extraction, which reveal that the extent of Ce anomaly is not a result of variations in redox conditions, but appears to be kinetically controlled, decreasing as growth rate increases from hydrogenetic to diagenetic to hydrothermal oxides [40].

## 5. Conclusions

A unique set of Co-poor hydrogenetic nodules collected from the Philippine Sea, located on both sides of the Kyushu–Palau ridge at water depths of 4400–6000 m, show characteristics unlike typical hydrogenetic nodules from other regions. Through comprehensive and detailed studies, we have recognized the diversity controls on critical metal enrichments in these hydrogenetic Fe–Mn nodules. The enrichments basically depend on the type of genetic process: hydrogenetic and diagenetic. The diagenetic layers (Mn-rich layers) and high Mn/Fe ratios in deep-water nodules show a diagenetic signal but a positive Ce anomaly, which constrains the diagenetic redox conditions to early oxic diagenesis.

This additional diagenetic source enhanced the Mn, Li, Ni, and Cu contents in deep-water nodules. In contrast, Fe-rich layers and high Fe metals in the shallower-water nodules might depend on the supply of Fe oxyhydroxide from CCD. The supply of iron hydroxide has a diluting effect on Mn, Ni, and Co but an enrichment effect on Fe and REE in nodules near topographic highs.

High-resolution analyses of element contents reveal complex element associations among the critical metals, which are not resolvable through conventional bulk analytical techniques. Co is positively related to Mn content in hydrogenetic layers, while negatively correlated with Mn in diagenetic layers. As a result, the low Co contents of the ‘pure hydrogenetic’ shallower-water nodules can be attributed to the low Mn contents (high Fe contents), and the low Co contents in the deep-water nodules are caused by diagenetic Mn origin from pore water in the sediments.

The growth rate of the Fe–Mn oxyhydroxides might control the enrichment of REE, which is consistent with the finding for Co. However, although Co and REE have similar behavior in that their enrichments are negative to growth rate, some differences exist related to their absorptions. Co is adsorbed at the surfaces of MnO<sub>2</sub> colloids, while REE enter both Fe phases and Mn phases. Thus, Co is positively related to Mn content in ‘pure hydrogenetic layers’ when the growth rates are low, but REE shows similar contents in ‘pure hydrogenetic layers’, no matter whether in Fe-rich layers (high Fe/Mn ratio) or normal layers (Fe/Mn = ~1).

Our findings suggest that comprehensive and detailed studies can be an effective approach for expanding our understanding of the diverse genetic processes, as well as identifying the influence of local, regional, or global changes in mass-water chemistry, element inputs, and environmental factors affecting the nodule growth.

**Supplementary Materials:** The following Supporting Materials can be downloaded at: <https://www.mdpi.com/article/10.3390/min13040522/s1>, Figure S1: The cross sections of the nodules; Table S1: Locations and depths of the samples; Table S2: Trace element compositions obtained using LA-ICP-MS. Table S3: Test chemical compositions values of the standard materials (XRF and ICP-MS).

**Author Contributions:** Conceptualization, C.L. and S.-J.K.; methodology, W.S.; formal analysis, C.L. and W.S.; software, Z.S., C.L., and X.Y.; investigation, G.H. and C.L.; data curation, W.S.; resources, W.S. and S.-J.K.; writing—original draft preparation, C.L.; writing—review and editing, W.S. and S.-J.K.; visualization, C.L.; supervision, S.-J.K. and W.S.; project administration, W.S. and S.-J.K. All authors have read and agreed to the published version of the manuscript.

**Funding:** This research was supported by National Natural Science Foundation of China (grant 92058204), China Geological Survey (grant DD20221720 and DD20190236), and Key laboratory of submarine geosciences, MNR (grant KLSG2005).

**Conflicts of Interest:** The authors declare no conflict of interest.

## References

1. Hein, J.R.; Koschinsky, A. Deep-Ocean Fe–Mn Crust and Nodules. In *Earth Systems and Environmental Sciences, Treatise on Geochemistry*, 2nd ed.; Holland, H., Turekian, K., Eds.; Elsevier: Amsterdam, The Netherlands, 2013; pp. 273–291.
2. Kuhn, T.; Wegorzewski, A.; Rühlemann, C.; Vink, A. Composition, Formation, and Occurrence of Polymetallic Nodules. In *Deep-Sea Mining: Resource Potential, Technical and Environmental Considerations*; Sharma, R., Ed.; Springer International Publishing: Berlin/Heidelberg, Germany, 2017; pp. 23–63.
3. Hein, J.R.; Koschinsky, A.; Kuhn, T. Deep-ocean polymetallic nodules as a resource for critical materials. *Nat. Rev. Earth Environ.* **2020**, *1*, 158–169. [[CrossRef](#)]
4. Marino, E.; González, F.J.; Lunar, R.; Reyes, J.; Medialdea, T.; Castillo-Carrión, M.; Bellido, E.; Somoza, L. High-Resolution Analysis of Critical Minerals and Elements in Fe–Mn Crusts from the Canary Island Seamount Province (Atlantic Ocean). *Minerals* **2018**, *8*, 285. [[CrossRef](#)]
5. Kuhn, T.; Heller, C.; Kasten, S.; Koschinsky, A.; Versteegh, G.; Villinger, H. Niedrigthermale Fluidzirkulation an Seamounts und Störungszonen in 20 Mio. Jahre alter ozeanischer Kruste: Ergebnisse der Expedition SO240-FLUM. Statusseminar “Meeresforschung mit FS SONNE”. In Proceedings of the Tagungsband zum Statusseminar 2017 Meeresforschung mit FS Sonne, Oldenburg, Germany, 14–15 February 2017; pp. 30–34.

6. Dutkiewicz, A.; Judge, A.; Müller, D. Environmental predictors of deep-sea polymetallic nodule occurrence in the global ocean. *Geology* **2020**, *48*, 293–297. [[CrossRef](#)]
7. Josso, P.; Rushton, J.; Lusty, P.; Matthews, A.; Chenery, S.; Holwell, D.; Kemp, S.J.; Murton, B. Late Cretaceous and Cenozoic paleoceanography from north-east Atlantic Fe–Mn crust microstratigraphy. *Mar. Geol.* **2020**, *422*, 106122. [[CrossRef](#)]
8. Ren, J.B.; Yao, H.Q.; Yang, Y.; Wang, L.X.; He, G.W.; Lai, P.X.; Zhou, J.; Deng, X.G.; Liu, S.J.; Deng, X.Z.; et al. Critical metal enrichment in atypical hydrogenetic Fe–Mn nodules: A case study in the Central Basin Ridge of the West Philippine Basin. *Chem. Geol.* **2023**, *615*, 121224. [[CrossRef](#)]
9. González, F.J.; Somoza, L.; Hein, J.R.; Medialdea, T.; León, R.; Urgorri, V.; Reyes, J.; Martín-Rubí, J.A. Phosphorites, Co-rich Mn nodules, and Fe–Mn crusts from Galicia Bank, NE Atlantic: Reflections of Cenozoic tectonics and paleoceanography. *Geochem. Geophys. Geosyst.* **2016**, *17*, 346–374. [[CrossRef](#)]
10. Marino, E.; González, F.J.; Somoza, L.; Lunar, R.; Ortega, L.; Vázquez, J.T.; Reyes, J.; Bellido, E. Strategic and rare elements in Cretaceous–Cenozoic cobalt-rich ferromanganese crusts from seamounts in the Canary Island Seamount Province (northeastern tropical Atlantic). *Ore Geol. Rev.* **2017**, *87*, 41–61. [[CrossRef](#)]
11. Halbach, P.; Friedrich, G.; von Stackelberg, U. *The Manganese Nodule Belt of the Pacific Ocean*; Enke: Stuttgart, Germany, 1988; pp. 61–69.
12. Wegorzewski, A.V.; Dutkiewicz, T. The influence of suboxic diagenesis on the formation of manganese nodules in the Clarion Clipperton nodule belt of the Pacific Ocean. *Mar. Geol.* **2014**, *357*, 123–138. [[CrossRef](#)]
13. Usui, A.; Graham, I.J.; Ditchburn, R.G.; Zondervan, A.; Shibasaki, H.; Hishida, H. Growth history and formation environments of Fe–Mn deposits on the Philippine Sea Plate, Northwest Pacific Ocean. *Isl. Arc.* **2007**, *16*, 420–430. [[CrossRef](#)]
14. Zhou, J.; Cai, P.J.; Yang, C.P.; Liu, S.F.; Luo, W.D.; Nie, X. Geochemical characteristics and genesis of Fe–Mn nodules and crusts from the Central Rift Seamounts Group of the West Philippine Sea. *Ore Geol. Rev.* **2022**, *145*, 104923. [[CrossRef](#)]
15. Li, C.; Song, W.; Sun, Z.; Huang, W.; Hu, G.; Yuan, X.; Kao, S.-J. High-Resolution Analysis of Fe–Mn Oxyhydroxide in Ferromanganese Nodules from the Northwestern Pacific Ocean and Insights on Element Mobility. *Minerals* **2023**, *13*, 415. [[CrossRef](#)]
16. Liu, Y.S.; Hu, Z.C.; Gao, S.; Günther, D.; Xu, J. In situ analysis of major and trace elements of anhydrous minerals by LA-ICP-MS without applying an internal standard. *Chem. Geol.* **2008**, *257*, 34–43. [[CrossRef](#)]
17. Chen, L.; Liu, Y.S.; Hu, Z.C.; Gao, S.; Zong, K.Q.; Chen, H.H. Accurate determinations of fifty-four major and trace elements in carbonate by LA-ICP-MS using normalization strategy of bulk components as 100%. *Chem. Geol.* **2011**, *284*, 283–295. [[CrossRef](#)]
18. McLennan, S.M. Rare Earth Elements in Sedimentary Rocks: Influence of Provenance and Sedimentary Processes. In *Geochemistry and Mineralogy of Rare Earth Elements*; Lipin, B.R., McKay, G.A., Eds.; Mineralogical Society of America: Washington, MA, USA, 1989; Volume 21, pp. 169–200.
19. Hein, J.R.; Spinardi, F.; Okamoto, N.; Mizell, K.; Thorburn, D.; Tawake, A. Critical metals in manganese nodules from the Cook Islands EEZ, abundances and distributions. *Ore Geol. Rev.* **2015**, *68*, 97–116. [[CrossRef](#)]
20. Guan, Y.; Sun, X.M.; Shi, G.Y.; Jiang, X.D.; Lu, H.F. Rare earth elements composition and constraint on the genesis of the polymetallic crusts and nodules in the South China Sea. *Acta Geol. Sin. Engl. Ed.* **2017**, *91*, 1751–1766. [[CrossRef](#)]
21. Knaack, D.; Sullivan, K.; Brown, D.; Langa, M.; Mathieu, J.; Bouchard, M.; Haring, M.; Petrus, J.; Stern, B.; Hein, J.; et al. Geochemical and mineralogical composition of Fe–Mn precipitates from the southern Mariana arc: Evaluation, formation, and implications. *Chem. Geol.* **2021**, *568*, 120132. [[CrossRef](#)]
22. Ren, X.W.; Liu, J.H.; Shi, X.F.; Cui, Y.C.; Lin, X.H. Genesis and ore-forming stages of co-rich Fe–Mn crusts from seamount m of magellan seamounts: Evidence from geochemistry and co chronology. *Mar. Geol. Quat. Geol.* **2011**, *31*, 65–74. [[CrossRef](#)]
23. Su, R.; Sun, F.Y.; Li, X.H.; Chu, F.Y.; Sun, G.S.; Li, J.; Wang, H.; Li, Z.G.; Zhang, C.; Zhang, W.Y.; et al. Diverse early diagenetic processes of Fe–Mn nodules from the eastern Pacific Ocean: Evidence from mineralogy and in-situ geochemistry. *Int. Geol. Rev.* **2022**. ahead of print. [[CrossRef](#)]
24. Bonatti, E.; Kraemer, T.; Rydell, H. Classification and genesis of submarine iron-manganese deposits. In *Fe–Mn Deposits on the Ocean Floor*; Horn, D.R., Ed.; NSF: Washington, DC, USA, 1972; pp. 149–166.
25. Josso, P.; Pelleter, E.; Pourret, O.; Fouquet, Y.; Etoubleau, J.; Cheron, S.; Bollinger, C. A new discrimination scheme for oceanic Fe–Mn deposits using high field strength and rare earth elements. *Ore Geol. Rev.* **2017**, *87*, 3–15. [[CrossRef](#)]
26. Bau, M.; Schmidt, K.; Koschinsky, A.; Hein, J.; Kuhn, T.; Usui, A. Discriminating between different genetic types of marine ferro-manganese crusts and nodules based on rare earth elements and yttrium. *Chem. Geol.* **2014**, *381*, 1–9. [[CrossRef](#)]
27. Blöthe, M.; Wegorzewski, A.; Müller, C.; Simon, F.; Kuhn, T.; Schippers, A. Manganese-cycling microbial communities inside deep-sea manganese nodules. *Environ. Sci. Technol.* **2015**, *49*, 7692–7700. [[CrossRef](#)]
28. Hein, J.R.; Koschinsky, A.; Bau, M.; Manheim, F.T.; Kang, J.K.; Roberts, L. Co-rich Fe–Mn crusts in the Pacific. In *Handbook of Marine Mineral Deposits*; CRC Marine Science Series; Cronan, D.S., Ed.; CRC Press: Boca Raton, FL, USA, 2000; pp. 239–279.
29. Hein, J.R.; Koschinsky, A.; Halbach, P.; Manheim, F.T.; Bau, M.; Kang, J.K.; Lubick, N. Iron and manganese oxide mineralization in the Pacific. *Geol. Soc. Lond. Spec. Publ.* **1997**, *119*, 123–138. [[CrossRef](#)]
30. Wegorzewski, A.V.; Kuhn, T.; Dohrmann, R.; Wirth, R.; Grangeon, S. Mineralogical characterization of individual growth structures of Mn-nodules with different Ni + Cu content from the central Pacific Ocean. *Am. Mineral.* **2015**, *100*, 2497–2508. [[CrossRef](#)]

31. Marino, E.; González, F.J.; Kuhn, T.; Madureira, P.; Wegorzewski, A.V.; Mirao, J.; Medialdea, T.; Oeser, M.; Miguel, C.; Reyes, J.; et al. Hydrogenetic, Diagenetic and Hydrothermal Processes Forming Ferromanganese Crusts in the Canary Island Seamounts and Their Influence in the Metal Recovery Rate with Hydrometallurgical Methods. *Minerals* **2019**, *9*, 439. [[CrossRef](#)]
32. Halbach, P.; Hebisch, U.; Scherhag, C. Geochemical variations of Fe–Mn nodules and crusts from different provinces of the Pacific Ocean and their genetic control. *Chem. Geol.* **1981**, *34*, 3–17. [[CrossRef](#)]
33. Hein, J.R.; Mizell, K.; Koschinsky, A.; Conrad, T.A. Deep-ocean mineral deposits as a source of critical metals for high- and green-technology applications: Comparison with land-based resources. *Ore Geol. Rev.* **2013**, *51*, 1–14. [[CrossRef](#)]
34. Halbach, P.; Manheim, F.T. Potential of cobalt and other metals in Fe–Mn crusts on seamounts of the Central Pacific Basin. *Mar. Mining.* **1984**, *4*, 319–336.
35. Halbach, P. Processes controlling the heavy metal distribution in pacific Fe–Mn nodules and crusts. *Geol. Rundsch.* **1986**, *75*, 235–247. [[CrossRef](#)]
36. Usui, A.; Nishi, K.; Sato, H.; Nakasato, Y.; Thornton, B.; Kashiwabara, T.; Tokumaru, A.; Sakaguchi, A.; Yamaoka, K.; Kato, S.; et al. Continuous growth of hydrogenetic Fe–Mn crusts since 17 Myr ago on Takuyo-Daigo Seamount, NW Pacific, at water depths of 800–5500 m. *Ore. Geol. Rev.* **2017**, *87*, 71–87. [[CrossRef](#)]
37. Koschinsky, A.; Hein, J.R. Marine Fe–Mn encrustations: Archives of changing oceans. *Elements* **2017**, *13*, 177–182. [[CrossRef](#)]
38. Hein, J.R.; Koschinsky, A. Deep-ocean Fe–Mn crusts and nodules. In *Treatise on Geochemistry*; Scott, S., Ed.; Elsevier: New York, NY, USA, 2012; Volume 12.
39. Hein, J.R.; Conrad, T.A.; Frank, M.; Christl, M.; Sager, W.W. Copper-nickel-rich, amalgamated Fe–Mn crust-nodule deposits from Shatsky Rise, NW Pacific. *Geochem. Geophys. Geosyst.* **2012**, *13*, Q10022. [[CrossRef](#)]
40. Takahashi, Y.; Manceau, A.; Geoffroy, N.; Marcus, M.A.; Usui, A. Chemical and structural control of the partitioning of Co, Ce, and Pb in marine Fe–Mn oxides. *Geochim. Cosmochim. Acta* **2007**, *71*, 984–1008. [[CrossRef](#)]
41. Manheim, F.T. Marine cobalt resources. *Science* **1986**, *232*, 600–608. [[CrossRef](#)] [[PubMed](#)]
42. Halbach, P.E.; Jahn, A.; Cherkashov, G. Marine Co-Rich Fe–Mn Crust Deposits: Description and Formation, Occurrences and Distribution, Estimated World-wide Resources. In *Deep-Sea Mining: Resource Potential, Technical and Environmental Considerations*; Sharma, R., Ed.; Springer International Publishing: Berlin/Heidelberg, Germany, 2017; pp. 65–141.
43. Halbach, P.; Segl, M.; Puteanus, D.; Mangini, A. Co-fluxes and growth rates in Fe–Mn deposits from central Pacific seamount areas. *Nature* **1983**, *304*, 716–719. [[CrossRef](#)]
44. Sensarma, S.; Saha, A.; Hazra, A. Implications of REE incorporation and host sediment influence on the origin and growth processes of Fe–Mn nodules from Central Indian Ocean Basin. *Geosci. Front.* **2021**, *12*, 101123. [[CrossRef](#)]
45. Koschinsky, A.; Halbach, P. Sequential leaching of marine Fe–Mn precipitates: Genetic implications. *Geochim. Cosmochim. Acta* **1995**, *59*, 5113–5132. [[CrossRef](#)]
46. Koschinsky, A.; Hein, J.R. Uptake of elements from seawater by Fe–Mn crusts: Solid-phase associations and seawater speciation. *Mar. Geol.* **2003**, *198*, 331–351. [[CrossRef](#)]
47. Li, D.; Fu, Y.; Liu, Q.; Reinfelder, J.R.; Hollings, P.; Sun, X.; Tan, C.; Dong, Y.; Ma, W. High-resolution LA-ICP-MS mapping of deep-sea polymetallic micronodules and its implications on element mobility. *Gondwana Res.* **2020**, *81*, 461–474. [[CrossRef](#)]
48. Zhang, H.; Zhou, J.; Yuan, P.; Dong, Y.; Fan, W.; Chu, F.; Xiao, W.; Liu, D. Highly positive Ce anomalies of hydrogenetic ferromanganese micronodules from abyssal basins in the NW and NE Pacific: Implications for REY migration and enrichment in deep-sea sediments. *Ore. Geol. Rev.* **2023**, *154*, 105324. [[CrossRef](#)]
49. Bau, M. Scavenging of dissolved yttrium and rare earths by precipitating iron oxyhydroxide: Experimental evidence for Ce oxidation, Y–Ho fractionation, and lanthanide tetrad effect. *Geochim. Cosmochim. Acta* **1999**, *63*, 67–77. [[CrossRef](#)]

**Disclaimer/Publisher’s Note:** The statements, opinions and data contained in all publications are solely those of the individual author(s) and contributor(s) and not of MDPI and/or the editor(s). MDPI and/or the editor(s) disclaim responsibility for any injury to people or property resulting from any ideas, methods, instructions or products referred to in the content.